

Globally Optimal Finsler Active Contours

Christopher Zach, Liang Shan, and Marc Niethammer

University of North Carolina at Chapel Hill

Abstract. We present a continuous and convex formulation for Finsler active contours using seed regions or utilizing a regional bias term. The utilization of general Finsler metrics instead of Riemannian metrics allows the segmentation boundary to favor appropriate locations (e.g. with strong image discontinuities) and suitable directions (e.g. aligned with dark to bright image gradients). Strong edges are not required everywhere along the desired segmentation boundary due to incorporation of a regional bias. The resulting optimization procedure is simple and efficient, and leads to binary segmentation results regardless of the underlying continuous formulation. We demonstrate the proposed method in several examples.

1 Introduction

Image segmentation is one of the fundamental tasks in low level vision. In order to obtain general, efficient and globally optimal methods we focus on approaches using only *local* image information and disregard methods e.g. incorporating global foreground and background statistics leading to non-convex minimization tasks. We can identify several local influences determining the segmentation boundary between the foreground object and the background:

1. A regional bias, which favors either the foreground or background at particular image locations. The regional bias can be arbitrarily computed, and is understood as the log-likelihood ratio between the object and background probabilities.
2. A regularization force preferring smooth segmentation boundaries. We focus on regularizing the length (or area) of the segmentation boundary as induced by the underlying metric. This metric can be purely Euclidean or Riemannian with weights induced e.g. by strong image discontinuities.
3. A *strong* orientation force based on the total flux through the segmentation boundary favoring particular local orientations. By the divergence theorem (or by identifying the adjoint operator in the discrete setting) the flux term essentially modifies the regional bias locally by appropriate raising and decreasing the likelihood ratios. We denote the flux term as a strong force, since it is (as regional bias) always active in the energy functional regardless of the obtained segmentation boundary.
4. A *weaker* orientation force based on asymmetric Finsler metrics also favoring particular orientations but without modifying the regional bias. This term is only in effect at the segmentation boundary and does not contribute to the overall energy otherwise.

The synthetic example shown in Figure 1 illustrates the differences between the strong (flux-based) and the weaker (Finsler metric) orientation forces. Consider the input image shown in Figure 1(a): assume that the center region of the image is known to be inside the object and the image borders belong to the background (regional bias), and that the segmentation boundary between the objects interior and the background needs to coincide with a bright-to-dark transition in the image. Thus, the middle circle is the desired foreground boundary. A weighted Riemannian metric (which is always centrally symmetric) based on the strength of image edges generally favors the smallest segmentation result (Figure 1(b)). Adding the flux energy with weight γ either gives the Riemannian result, if γ is very small, the intended result for the right choice of γ , or leads to unintended segmentation results also showing spurious foreground pixels for large γ (due to the strong influence of the flux term on the regional bias, Figure 1(c–e)). Using a Finsler metric with weights as described in Section 3 yields the desired segmentation result (Figure 1(f)). Spurious foreground regions are never generated by Finsler metrics in locations without an appropriate regional bias.

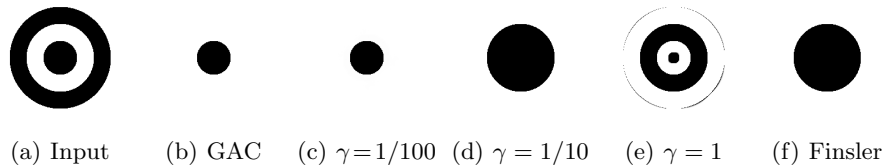


Fig. 1. Input image (a), Riemannian metric (GAC) segmentation result (b), flux-based segmentations with increasing weights for the flux term: $\gamma = 1/100$ (c), $\gamma = 1/10$ (d), and $\gamma = 1$ (e); and segmentation result using Finsler metrics (f).

2 Background

Segmentation boundaries generally coincide with strong edges in the source image, and a suitable weighting of the boundary term based on image gradient magnitudes leads to geodesic active contours (GAC) [1] and surfaces [2] optimizing a energy functional of the form

$$E(S) = \int_S w(S) dS, \quad (1)$$

where S represents the contour/surface with appropriate parametrization. In order to avoid the trivial solution with vanishing S , suitable endpoint or seed region constraints are required if a globally optimal solution is sought. A common choice for the weight function w is

$$w = \frac{1}{1 + \alpha \|\nabla I \sigma\|^p} + \epsilon, \quad (2)$$

where I^σ is a denoised (smoothed) version of the input image I , p is a shape parameter (usually $p = 1$ or $p = 2$), and $\alpha, \epsilon > 0$. If seed regions definitely belonging to the foreground and the background are known, then minimizing Eq. 1 corresponds to separating the seed regions with minimal boundary costs. Globally optimal minimizers for this segmentation task can be found using combinatorial methods [3] and a continuous formulation [4]. The energy in Eq. 1 only attracts the segmentation boundary to favor locations e.g. with large image gradients, but does not lead to preferred local boundary orientations. Such preference of particular directions can be achieved by using a flux-based term [5, 6], or by utilization of a position and direction dependent weighting function. Utilizing Finsler metrics for tractography is proposed in [7, 8], where the isotropic weighting function $w(\cdot)$ in Eq. 1 is replaced by $w(S, \mathcal{N}(S))$ (with $\mathcal{N}(S)$ denoting the normal direction to the curve S):

$$E(S) = \int_S w(S, \mathcal{N}(S)) dS. \quad (3)$$

Since the desired result is a curve in higher dimensions, a dynamic programming approach is employed to determine the minimizer of Eq. 3 (subject to endpoint constraints). The weight function w is not required to be a convex function, but the solution procedure implicitly convexifies w . Our proposed method (Section 3) can be understood as a globally optimal approach for Finsler active contour segmentation with (optional) region-based terms.

Kolmogorov and Boykov [9] present a globally optimal Finsler active contour approach based on graph cut construction. Finsler metrics are discretized and approximated by a symmetric (Riemannian) part and an anti-symmetric, flux-based term. The latter term poses a problem (possibly leading to spurious foreground objects) if region-based likelihoods are added to the energy (recall Figure 1(e)).

The two-phase Chan-Vese energy (also known as active contours without edges) [10] combines regional foreground and background likelihoods with boundary regularization,

$$E(A, \rho_F, \rho_B) = \text{Per}(\partial A) + \int_A \rho_F dx + \int_{\Omega \setminus A} \rho_B dx \quad (4)$$

$$= \text{Per}(\partial A) + \int_\Omega \rho(x) \mathbf{1}_A dx + \text{const} \quad (5)$$

where A is a subset of Ω , $\text{Per}(\partial A)$ is the length of the boundary of A , and ρ_F and ρ_B are the negative foreground and background log-likelihoods given at every $x \in \Omega$. $\rho := \rho_F - \rho_B$ is the log-likelihood ratio. Remarkably, this model does not strongly rely on distinctive image edges to attract the segmentation boundary. The particular choice of $\rho_F = (f - c_1)^2$ and $\rho_B = (f - c_2)^2$ for a given source image f and unknown values c_1, c_2 yields the classic Chan-Vese energy,

$$E(A, c_1, c_2) = \text{Per}(\partial A) + \lambda \int_A (c_1 - f(x))^2 dx + \lambda \int_{\Omega \setminus A} (c_2 - f(x))^2 dx. \quad (6)$$

In the following we fix the log-likelihood ratios ρ in advance and optimize only over the set A . Local minimizers of Eq. 5 can be determined e.g. by the level set approach [10]. Chan et al [11] propose to determine the optimal set A indirectly through $u = \mathbf{1}_A$:

$$E(u) = \int_{\Omega} (\|\nabla u\| + \rho(x)u) dx. \quad (7)$$

In [11] it is shown that the constraint $u \in \{0, 1\}$ can be replaced by its LP-relaxation, $u \in [0, 1]$, resulting in a convex minimization problem (for fixed ρ). A globally optimal binary solution can be obtained by thresholding any minimizer of Eq. 7 subject to $u \in [0, 1]$. Bresson et al. [12] extend this result to the case of weighted total variation to favor segmentation boundaries at image discontinuities where existent. An alternating minimization scheme is proposed, which is based on the relaxation of Eq. 7,

$$E(u, v) = \int_{\Omega} (\|\nabla u\| + \frac{1}{2\theta}(u - v)^2 + \rho u) dx \quad (8)$$

subject to $v \in [0, 1]$. This energy is optimized by alternating steps: update u using Chambolle's dual approach for the ROF energy [13], and point-wise minimization for v . Our solution procedure does not rely on such convex relaxations.

3 Convex Formulation of Finsler Active Contours

In this section we replace the scalar weights in Eq. 7 by position and direction dependent weighting functions. The goal is to use a formulation incorporating region terms (i.e. forces favoring either foreground or background at particular positions) and boundary terms (forces attracting the segmentation boundary at certain positions with particular orientations). More formally, let $(\phi_x)_{x \in \Omega}$ be a family of positively 1-homogeneous functions and $\rho: \Omega \rightarrow \mathbb{R}$ a data cost function. We search for the minimizer of

$$E(u) = \int_{\Omega} \phi_x(\nabla u) + \rho u dx \quad \text{subject to } u \in [0, 1], \quad (9)$$

Common choices for ϕ_x are $\|\cdot\|$ (total variation) and $w(x)\|\cdot\|$ (weighted TV). But ϕ can be more complex, e.g. an anisotropic version of total variation [14]. Since every ϕ_x is positively 1-homogeneous, we can write $\phi_x(\xi) = \|\xi\| \phi_x(\frac{\xi}{\|\xi\|})$. Figure 2(a) and (b) illustrate potential shapes W_ϕ induced by ϕ . These shapes are also denoted as *Wulff shapes* [14]. If Ω is bounded, then the set of functions $\{u : \Omega \rightarrow [0, 1]\}$ is also bounded, and a global minimum is attained for the convex and continuous functional $E(u)$.

Prominent choices for $\rho(\cdot)$ are $\rho(x) = \lambda((c_1 - f(x))^2 - (c_2 - f(x))^2)$ for the Chan-Vese energy Eq. 6, and $\rho(x) = \lambda$ if $f(x) = 0$ and $\rho(x) = -\lambda$ for $f(x) = 1$ corresponding to the TV- L^1 energy with a binary input image, i.e.

$$E(u; f) = \int_{\Omega} \|\nabla u\| + \lambda|u - f| dx \quad \text{subject to } u \in [0, 1], \quad (10)$$

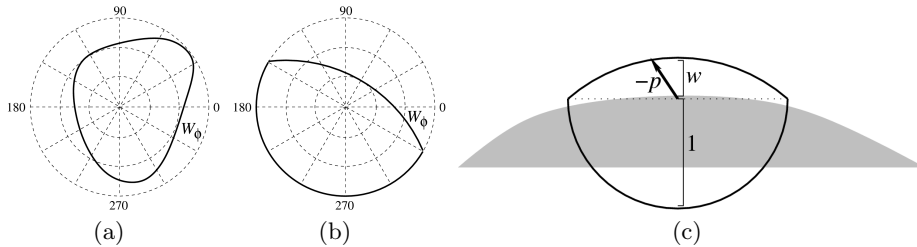


Fig. 2. General Wulff shape (a), the utilized shape for segmentation (b), and its alignment with image gradients (c).

with $f : \Omega \rightarrow \{0, 1\}$ (see [15]). Allowing ρ to be an extended function $\rho : \Omega \rightarrow \mathbb{R} \cup \{-\infty, +\infty\}$ also enables the incorporation of strict constraints $u(S) = 1$ and $u(T) = 0$ for source and sink regions $S, T \subseteq \Omega$. If ρ is zero in $\Omega \setminus (S \cup T)$, we arrive at a convex formulation of Finsler active contours (Eq. 3).

Without the regularization term, an optimal solution is simply given by $u = \mathbf{1}_{\{x:\rho(x)<0\}}$. The essentially binary nature of solution of Eq. 9 was already shown for the unweighted total variation [11] and weighted TV [12] (by rewriting the total variation in terms of the level sets of u). We give an alternative proof based on strong duality in convex analysis that directly extends to general families of convex, positively 1-homogeneous functions ϕ_x :

Theorem 1 *Let ϕ be a positively 1-homogeneous function, and $\rho : \Omega \rightarrow \mathbb{R}$. Then any global minimizer of Eq. 9 can be converted into a purely binary global minimizer by thresholding with an arbitrary value $\theta \in (0, 1)$.*

Proof: Assume $u^* : \Omega \rightarrow [0, 1]$ is a minimizer of Eq. 9. The corresponding thresholded binary function \hat{u} is given by

$$\hat{u}(\mathbf{x}) = \begin{cases} 1 & \text{if } u^*(\mathbf{x}) \geq \theta \\ 0 & \text{otherwise.} \end{cases}$$

First note, that $\nabla \hat{u} \neq 0$ only at the θ -level set, where it has the same direction as ∇u^* . Thus, we can write $\nabla \hat{u} = c \nabla u^*$ (point-wise) for $c \geq 0$.

The dual energy of Eq. 9 is given by (we omit the straightforward calculation to due lack of space)

$$E^*(\mathbf{p}) = \int_{\Omega} \min(0, \operatorname{div} \mathbf{p} + \rho) dx, \quad (11)$$

which is maximized with respect to a vector field \mathbf{p} subject to $-\mathbf{p} \in W_{\phi_x}$. W_{ϕ_x} is the convex Wulff shape induced by ϕ_x . By inserting the respective constraints on u and \mathbf{p} using the δ function, the primal and dual energies Eq. 9 and Eq. 11

can be stated as

$$E(u) = \int_{\Omega} \phi(\nabla u) + \rho u + \delta_{[0,1]}(u) dx \quad (12)$$

$$E^*(\mathbf{p}) = \int_{\Omega} \min(0, \operatorname{div} \mathbf{p} + \rho) - \delta_{W_{\phi}}(-\mathbf{p}) dx, \quad (13)$$

where we also drop the explicit dependence on x for ϕ . We employ the KKT conditions to show the optimality of \hat{u} [16]. Let \mathbf{p}^* be the corresponding dual solution for u^* . The KKT conditions for our particular minimization task are given by

$$\nabla u^* \in \partial \int \delta_{W_{\phi}}(-\mathbf{p}^*) dx \quad \text{and} \quad -\operatorname{div} \mathbf{p}^* \in \partial \int \rho u^* + \delta_{[0,1]}(u^*) dx. \quad (14)$$

The terms under the integral are independent, hence the KKT conditions can be applied point-wise. Therefore, (u^*, \mathbf{p}^*) are minimizers of $E(u)$ (Eq. 9) and the corresponding dual energy if and only if

$$\nabla u^* \in \partial(\delta_{W_{\phi}}(-\mathbf{p}^*)) \quad \text{and} \quad -\operatorname{div} \mathbf{p}^* \in \partial(\rho u^* + \delta_{[0,1]}(u^*)). \quad (15)$$

First, we show $\nabla \hat{u} \in \partial(\delta_{W_{\phi}}(-\mathbf{p}^*))$. The definition of the subgradient reads as

$$\delta_{W_{\phi}}(-\mathbf{p}^*) + (\nabla \hat{u})^T(\mathbf{p} - \mathbf{p}^*) \leq \delta_{W_{\phi}}(-\mathbf{p}).$$

Since \mathbf{p}^* is feasible and the inequality is trivially true for every $-\mathbf{p} \notin W_{\phi}$, we can assume $-\mathbf{p}^*$ and $-\mathbf{p}$ are in W_{ϕ} , i.e. $\delta_{W_{\phi}}(-\mathbf{p}^*) = 0$ and $\delta_{W_{\phi}}(-\mathbf{p}) = 0$. But

$$(\nabla \hat{u})^T(\mathbf{p} - \mathbf{p}^*) = c(\nabla u^*)^T(\mathbf{p} - \mathbf{p}^*) \leq 0, \quad (16)$$

since $c \geq 0$ by construction. Hence, $\nabla \hat{u}$ is also a subgradient of $\delta_{W_{\phi}}(-\mathbf{p}^*)$.

Next, we prove $-\operatorname{div} \mathbf{p}^* \in \partial(\rho \hat{u} + \delta_{[0,1]}(\hat{u}))$. If u^* is already either 0 or 1, then $\hat{u} = u^*$ and there is nothing to show. If u^* is in the open interval $(0, 1)$, then $\partial \delta_{[0,1]}(u^*)$ is 0, since $\delta_{[0,1]}(\cdot)$ is constant in $[0, 1]$. Further, the mapping $u \mapsto \rho u$ is smooth, and the the gradient is the only subgradient, i.e. $-\operatorname{div} \mathbf{p}^* \in \{\partial(\rho u^*)\} = \{\rho\}$. In order to prove that $-\operatorname{div} \mathbf{p}^*$ is a subgradient of $u \mapsto \rho \hat{u} + \delta_{[0,1]}(\hat{u})$ we have to show that

$$\rho \hat{u} + \delta_{[0,1]}(\hat{u}) - (\operatorname{div} \mathbf{p}^*)(u - \hat{u}) \leq \rho u + \delta_{[0,1]}(u) \quad (17)$$

for every u . But

$$\begin{aligned} & \rho \hat{u} + \delta_{[0,1]}(\hat{u}) - (\operatorname{div} \mathbf{p}^*)(u - \hat{u}) \\ &= \rho \hat{u} - (\operatorname{div} \mathbf{p}^*)(u - \hat{u}) && [\delta_{[0,1]}(\hat{u}) = 0] \\ &= \rho \hat{u} + \rho(u - \hat{u}) && [-\operatorname{div} \mathbf{p}^* = \rho] \\ &= \rho u \leq \rho u + \delta_{[0,1]}(u), \end{aligned} \quad (18)$$

Hence, $-\operatorname{div} \mathbf{p}^*$ is a subgradient of $\rho \hat{u} + \delta_{[0,1]}(\hat{u})$, thus (\hat{u}, \mathbf{p}^*) also satisfies the KKT conditions and \hat{u} is therefore a global minimizer. \square

In finite settings where Ω is represented by a discrete grid, simple thresholding also modifies the level lines, i.e. we have only $\nabla(\hat{u}) \approx c\nabla u^*$. Thus, pure thresholding in the discrete setting yields to (slightly) inferior energies for \hat{u} .

By utilization of $\phi(\nabla u) = \max_{\mathbf{p} \in W_\phi} (-\mathbf{p}^T \nabla u)$, where W_ϕ is the convex Wulff shape induced by ϕ , we rewrite the energy Eq. 9 in a primal-dual setting (omitting the explicit dependence on x):

$$E(u) = \int_{\Omega} \max_{\mathbf{p} \in W_\phi} (-\mathbf{p}^T \nabla u) + \rho u \, dx \quad \text{subject to } u \in [0, 1], \quad (19)$$

and the respective gradient descent (in u) and ascent (for \mathbf{p}) equations are

$$\begin{aligned} \frac{\partial u}{\partial t} &= -\operatorname{div} \mathbf{p} - \rho & \text{s.t. } u \in [0, 1] \\ \frac{\partial \mathbf{p}}{\partial t} &= -\nabla u & \text{s.t. } -\mathbf{p} \in W_\phi \end{aligned} \quad (20)$$

for the artificial time parameter t . Enforcing the constraints on u and \mathbf{p} is simply done by clamping $u(x)$ to $[0, 1]$, and reprojecting $\mathbf{p}(x)$ onto the feasible set W_{ϕ_x} . Standard stability arguments establish the maximal stable timestep $\tau < 1/\sqrt{K}$, where K is the dimension of Ω (i.e. 2 for images). These equations have a similar structure as the continuous maximal flow equations [4], but differ substantially from the solution procedure proposed in [12] for direction independent (isotropic) functions ϕ_x based on Eq. 8.

There is a wide range of possibilities how to design ϕ_x (or the respective Wulff shape W_{ϕ_x}). The Wulff shape depicted in Figure 2(b), composed by a half-circle (with radius 1) and a circular segment (with height w), naturally combines gradient direction with gradient magnitude. The orientation of the shape is aligned with ∇I (Figure 2(c)), and the respective height $w(x)$ is given by Eq. 2 with $p = 1$. Homogenous regions ($\|\nabla I(x)\| = 0$, i.e. $w(x) = 1$) lead to direction independent perimeter regularization, and strong edges ($w(x) \ll 1$) result in low cost if the boundary is locally aligned with the image discontinuity. The situation depicted in Figure 2(c) corresponds to $u = 1$ representing the foreground, and the shaded region indicating darker image values. This particular shape also allows very simple reprojection operations for \mathbf{p} after the gradient ascent update Eq. 20.

4 Results

4.1 Histology Segmentation

The prototypical example for Finsler active contours is the segmentation of thick-walled anatomical structures like blood vessels in histology slides, see Figure 3. Given foreground seeds inside the lumen of the artery, geodesic active contours (i.e. with isotropic weighting of the contour length) generally return the inner wall of the artery as segmentation result (Figure 3(a)). Incorporating knowledge on the expected intensity gradient (going from dark to bright) using the proposed asymmetric Finsler metric as depicted in Figure 2(c) aligns the segmentation boundary with the exterior wall of the vessel, see Figure 3(b).

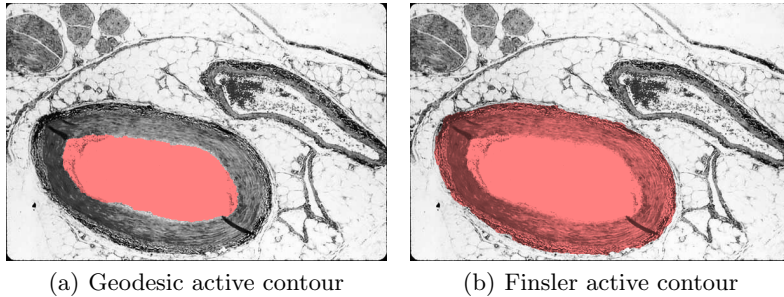


Fig. 3. Result of vessel segmentation in histology slides using geodesic active contours (a) and Finsler active contours (b). [Best viewed in color. Image data courtesy of Prof. David King, <http://www.siumed.edu/~dking2/crr/>.]

4.2 Bone Segmentation

We apply the proposed method on a bone segmentation task given MR images of the knee joint. Cortical bone appears black in both T1 and T2 weighted MR images, whereas muscles and tissues appear bright. Hence, a proper bone segmentation boundary runs through a dark-to-bright intensity transition. Consequently, the correct segmentation boundary is often not solely induced by the strongest edge in T1 and T2 weighted images. In order to obtain the regional bias ρ , we compute the likelihoods $p(I_{T_1}, I_{T_2} | \textit{bone})$ and $p(I_{T_1}, I_{T_2} | \textit{background})$ for the Bayesian classifier based on a non-parametric estimation of the joint histogram of T1 and T2 intensities for foreground (bone) and background (everything else). Prior to the computation of the histograms, we mask out the image background followed by MR bias field correction using the MNI’s N3 algorithm [17]. The data samples for kernel density estimation to derive the respective probabilities are obtained by a user-guided segmentation of one test-case.

Figure 4 shows the segmentation results using the isotropic Riemannian metric (GAC) approach (b) and the proposed Finsler metric method (c). Both intensity gradients in the T1 and T2 images are used to obtain the weighting function (Eq. 2) with $\alpha = 20$. The only difference in the settings between the Riemannian and the Finsler approach is the utilization of direction dependent weighting $\phi_{\mathbf{x}}$ as induced by the shape depicted in Figure 2(c). Note the “eroded” bone segmentation result returned by standard geodesic active contours in Figure 4(b).

4.3 Run-Time Performance for the Chan-Vese Model

The proposed procedure (Eq. 20) is in practice also more efficient than the convex relaxation approach, Eq. 8. We compared the run-time performance of the primal-dual scheme Eq. 20 with the performance of the relaxation approach Eq. 8 proposed in [12] for the standard Chan-Vese model (Eq. 6). Figure 5 displays the 256×256 input image, the segmentation result using black and white for c_1 and c_2 , respectively, and the corresponding primal and dual energies.

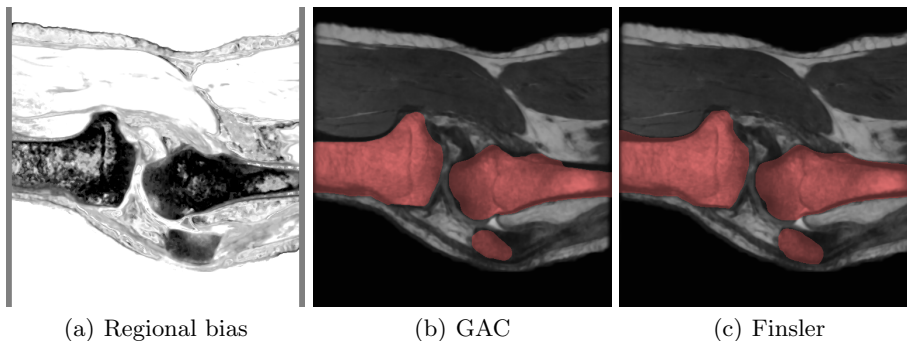


Fig. 4. Regional bias—dark regions indicate likely bone structure (a). T2 image and overlaid bone segmentation results using Riemannian metrics (b) and Finsler metrics (c). [Best viewed in color. Image data courtesy of Duke Image Analysis Laboratory (<http://dial.mc.duke.edu>).]

The data weight λ is set to 4. The run-time for one iteration is very similar in both methods, hence we display the evolution of primal and dual energies with respect to the iteration number. With GPU acceleration, real-time performance even for the iterated approach successively updating the means c_1 and c_2 can be obtained.

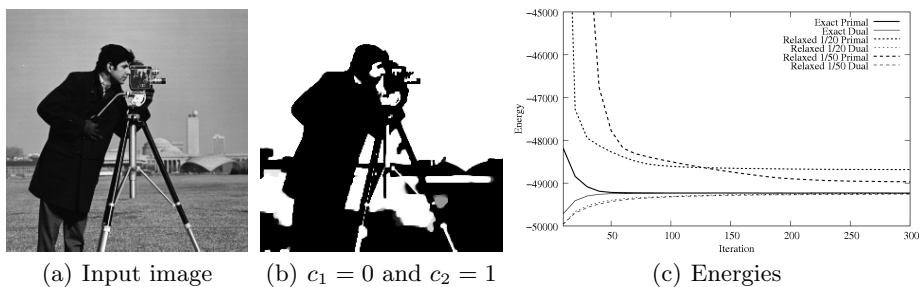


Fig. 5. (a) input image; (b) segmentation result with $c_1 = 0$ and $c_2 = 1$; (c) primal and dual energies (with respect to the iteration number) of the proposed method (solid lines) and the relaxation approach [12] (dashed lines).

5 Conclusion

We developed a continuous and convex formulation for binary segmentation tasks incorporating a regional term and a position and orientation dependent prior for the segmentation boundary represented by Finsler metrics. Finsler active contours provide an alternative approach to incorporate image-based priors

on the location and orientation of the segmentation boundary. The continuous relaxation yields an efficient solution method highly suitable for data-parallel implementations. Nevertheless, global optimal binary segmentation results are obtained in the continuous framework.

Future work will address extending the class of energies that can be optimized in the convex and continuous framework. For instance, the continuous formulation for length ratio minimization given in [18] can be easily extended to Finsler metrics.

References

1. Caselles, V., Kimmel, R., Sapiro, G.: Geodesic active contours. *IJCV* **22**(1) (1997) 61–79
2. Caselles, V., Kimmel, R., Sapiro, G., Sbert, C.: Minimal surfaces based object segmentation. *IEEE Trans. Pattern Anal. Mach. Intell.* **19** (1997) 394–398
3. Boykov, Y., Kolmogorov, V.: Computing geodesics and minimal surfaces via graph cuts. In: *Proc. ICCV.* (2003) 26–33
4. Appleton, B., Talbot, H.: Globally minimal surfaces by continuous maximal flows. *IEEE Trans. Pattern Anal. Mach. Intell.* **28**(1) (2006) 106–118
5. Vasilevskiy, A., Siddiqi, K.: Flux maximizing geometric flows. *IEEE Trans. Pattern Anal. Mach. Intell.* **24**(12) (2002) 1565–1578
6. Kimmel, R., Bruckstein, A.: Regularized Laplacian zero crossings as optimal edge integrators. *IJCV* **53**(3) (2003) 225–243
7. Pichon, E., Westin, C.F., Tannenbaum, A.: A Hamilton-Jacobi-Bellman approach to high angular resolution diffusion tractography. In: *Proc. MICCAI.* (2005) 180–187
8. Melonakos, J., Pichon, E., Angenent, S., Tannenbaum, A.: Finsler active contours. *IEEE Trans. Pattern Anal. Mach. Intell.* **30**(3) (2008) 412–423
9. Kolmogorov, V., Boykov, Y.: What metrics can be approximated by geo-cuts, or global optimization of length/area and flux. In: *Proc. ICCV.* (2005) 564–571
10. Chan, T.F., Vese, L.: Active contours without edges. *IEEE Trans. Image Processing* **10**(2) (2001) 266–277
11. Chan, T.F., Esedoglu, S., Nikolova, M.: Algorithms for finding global minimizers of image segmentation and denoising models. *SIAM Journal on Applied Mathematics* **66**(5) (2006) 1632–1648
12. Bresson, X., Esedoglu, S., Vandergheynst, P., Thiran, J., Osher, S.: Fast Global Minimization of the Active Contour/Snake Model. *J. Math. Imag. Vision* (2007)
13. Chambolle, A.: An algorithm for total variation minimization and applications. *J. Math. Imag. Vision* **20**(1–2) (2004) 89–97
14. Osher, S., Esedoglu, S.: Decomposition of images by the anisotropic Rudin-Osher-Fatemi model. *Comm. Pure Appl. Math.* **57** (2004) 1609–1626
15. Chan, T.F., Esedoglu, S.: Aspects of total variation regularized L^1 function approximation. *SIAM Journal on Applied Mathematics* **65**(5) (2004) 1817–1837
16. Borwein, J., Lewis, A.S.: *Convex Analysis and Nonlinear Optimization: Theory and Examples.* Springer (2000)
17. Sled, J.G., Zijdenbos, A.P., Evans, A.C.: A non-parametric method for automatic correction of intensity non-uniformity in MRI data. *IEEE Transactions on Medical Imaging* **17** (1998) 87–97
18. Kolev, K., Cremers, D.: Continuous ratio optimization via convex relaxation with applications to multiview 3D reconstruction. In: *Proc. CVPR.* (2009)